Materials Advances

ROYAL SOCIETY OF CHEMISTRY

PAPER

View Article Online
View Journal | View Issue

Cite this: *Mater. Adv.*, 2026, 7, 5136

Luminescent thermometry in $NaSrY(MoO_4)_3:Tm^{3+}/Yb^{3+}$: achieving high thermal sensitivities across the visible and near-infrared-I/III windows

Mariem Yangui,[a] Kamel Saidi,[ab]* Christian Hernández-Álvarez,[c] Mohamed Dammak[a] and I. R. Martín[c]

Remote optical thermometry has garnered significant attention due to its non-contact nature, high sensitivity, and rapid response capabilities, which are essential for industrial and biomedical applications. Lanthanide-doped luminescent materials, particularly Tm^{3+}-based systems, represent promising candidates for such thermometers owing to their tunable, temperature-dependent emissions and strong luminescence across biological transparency windows. Herein, Tm^{3+}/Yb^{3+} co-doped $NaSrY(MoO_4)_3$ (NSYM) phosphors were synthesized *via* a sol–gel method. Under 975 nm excitation, the material exhibits upconversion emissions at 487 nm ($^1G_4 \rightarrow {}^3H_6$) and 693 nm ($^1G_4 \rightarrow {}^3F_4$), alongside near infrared (NIR) emissions at 797 nm ($^3H_4 \rightarrow {}^3H_6$; NIR-I) and 1625 nm ($^3F_4 \rightarrow {}^3H_6$; NIR-III). Additionally, it shows a band at 1450–1550 nm ($^3H_4 \rightarrow {}^3F_4$; NIR-III) enabling simultaneous operation across the visible spectrum as well as the first and third biological transparency windows. The luminescence intensity ratios (LIRs) of 693/487 nm (LIR3), 693/663 nm (LIR2), and 1625/1500 nm (LIR8) yield exceptional relative thermal sensitivities of 1.84% K^{-1}, 1.90% K^{-1}, and 0.82% K^{-1}, respectively. Notably, LIR3 operates within the third biological window (NIR-III), where tissue penetration is maximized, rendering it particularly valuable for deep-tissue applications. The system demonstrates temperature uncertainties as low as 0.4–0.5 K over the 297–356 K range, significantly outperforming most of the reported luminescent nanothermometers. Furthermore, strong NIR-III emission under low excitation power underscores the potential of NSYM:Tm^{3+}/Yb^{3+} for deep-tissue imaging, optical signal amplification, and non-invasive biological thermometry. These results establish Tm^{3+}-based phosphors as highly promising platforms for next-generation optical thermal sensors in biomedicine.

Received 6th February 2026,
Accepted 9th April 2026

DOI: 10.1039/d6ma00173d

rsc.li/materials-advances

1. Introduction

Remote optical nanothermometry has emerged as a powerful tool for non-invasive temperature sensing in biological systems, with critical applications in photothermal therapy, photodynamic therapy, and real-time monitoring of cellular.[1,2] Unlike conventional thermometers, optical nanothermometers offer high spatial resolution, fast response times, and the ability to provide real-time thermal mapping without physical contact.[3] Among various platforms, lanthanide-doped luminescent nanoparticles (LNPs) stand out due to their exceptional photostability, absence of blinking, and rich emission spectra spanning ultraviolet to near-infrared (NIR).[4–7] Temperature readout in LNPs can be achieved through multiple optical parameters, such as emission intensity, spectral shift, lifetime, or luminescence intensity ratio (LIR). Of these, LIR and lifetime-based methods are particularly robust, as they are largely immune to fluctuations in excitation power, probe concentration, or environmental scattering factors that commonly compromise accuracy in biological systems.[8,9]

A major challenge in *in vivo* thermometry lies in the strong absorption and scattering of light by biological tissues.[10] To maximize penetration depth and imaging fidelity, optical nanothermometers must operate within the biological transparency windows: NIR-I (650–950 nm), NIR-II (1000–1350 nm), and NIR-III (1500–1850 nm).[11] Emissions in the NIR-II/III regions are especially advantageous, offering up to 100-fold improvements in the signal-to-noise ratio, enhanced spatial resolution, and deeper tissue penetration compared to visible or NIR-I probes.[12–16] Despite these advantages, a critical limitation persists in the field: the vast majority of reported lanthanide-based

[a] *Laboratoire de Physique Appliquée, Groupe des Matériaux Luminescents, Faculté des Sciences de Sfax, Département de Physique, Université de Sfax, BP 1171 Sfax, Tunisia*
[b] *University of Sfax, Department of Physics, Sfax Preparatory Engineering Institute, 1172 - 3000Sfax, Tunisia. E-mail: saidikamel494@gmail.com*
[c] *Universidad de La Laguna, Departamento de Física, and IMN Apdo. Correos 456, E-38206San Cristóbal de La Laguna, Santa Cruz de Tenerife, Spain*

optical nanothermometers operate effectively in only one biological window, typically NIR-I, while lacking usable emission in the deeper-penetrating NIR-II and NIR-III regions. To broaden the spectral coverage, some research groups have employed tri-doped systems (*e.g.*, $Yb^{3+}/Er^{3+}/Tm^{3+}$ or $Yb^{3+}/Ho^{3+}/Tm^{3+}$), as demonstrated by Jaque, Carlos and Marcin *et al.*[17–19] While these approaches can extend emission into multiple windows, they often introduce synthetic complexity, competing energy-transfer pathways, and reduced efficiency in the NIR-III region particularly under low-power excitation compatible with biological safety limits. Even among Tm^{3+}-based systems, which theoretically support multi-window emission, practical implementations frequently suffer from weak NIR-III luminescence, low thermal sensitivity in the NIR range, or reliance on high excitation densities. Furthermore, most ratiometric thermometry strategies remain confined to visible or NIR-I transitions, failing to exploit the full potential of Tm^{3+}'s rich energy-level structure for deep-tissue.[2,20–22] Tm^{3+}-based systems present a compelling alternative. When sensitized by Yb^{3+}, Tm^{3+} exhibits a cascade of radiative transitions spanning the visible to NIR-III range. This unique multi-window capability, rare among lanthanides, enables simultaneous operation across all three biological transparency windows.[23,24] Although non-radiative losses can occur due to the small energy gap between the $^3H_4$ and $^3H_5$ levels, strategic host selection and efficient $Yb^{3+} \rightarrow Tm^{3+}$ energy transfer can significantly enhance NIR quantum efficiency.[25–27] Moreover, the two-photon upconversion process in these systems efficiently populates the $^3H_4$ state, enabling strong NIR-III emission under low-power 975 nm excitation superior to other lanthanides such as Ho^{3+}, Er^{3+}, or Pr^{3+} in this spectral region.[6,28–31] Nevertheless, to date, no Tm^{3+}-based nanothermometer has successfully combined (i) high ratiometric thermal sensitivity in the physiological temperature range and (ii) strong and stable emission across all three biological windows, especially the underutilized NIR-III band.

Herein, we address this gap by developing Tm^{3+}/Yb^{3+} co-doped $NaSrY(MoO_4)_3$ (NSYM) phosphors *via* a sol–gel method. Our material achieves intense, temperature-sensitive luminescence across the visible, NIR-I, and NIR-III regions, simultaneously covering the most important biological transparency windows using only two dopant ions while delivering exceptional thermal sensitivities (1.84–1.90% K^{-1} and 0.82% K^{-1}, respectively) and remarkably low temperature uncertainties (0.4–0.5 K) under biocompatible excitation conditions. Notably, the pronounced NIR-III emission is particularly valuable, as this third biological window maximizes tissue penetration, rendering it the most advantageous spectral region for deep *in vivo* applications. This work establishes a simplified yet high-performance platform for next-generation optical nanothermometers in deep-tissue diagnostics and advanced thermal sensors in biomedicine.

2. Experimental section

2.1. Materials and synthesis

All reagents were purchased from Sigma-Aldrich (St. Louis, MO, USA) and used as received without further purification. The starting materials included sodium nitrate ($NaNO_3$, 99.0%), strontium nitrate ($Sr(NO_3)_2{\cdot}5H_2O$, 99.9%), yttrium nitrate ($Y(NO_3)_3{\cdot}6H_2O$, 99.9%), ytterbium nitrate ($Yb(NO_3)_3{\cdot}5H_2O$, 99.9%), thulium nitrate ($Tm(NO_3)_3{\cdot}5H_2O$, 99.9%), ammonium heptamolybdate ($(NH_4)_6Mo_7O_{24}{\cdot}4H_2O$, 99.96%), citric acid ($C_6H_8O_7$, 99.0%), nitric acid ($HNO_3$, 65%), and deionized water (18.2 MΩ cm).

The Tm^{3+}/Yb^{3+} co-doped sodium strontium yttrium molybdate (NSYM) phosphors were prepared using a citric acid-assisted sol–gel route. Predetermined quantities of the metal nitrate precursors were dissolved in an aqueous acidic medium (5 mL of concentrated HNO_3 and 25 mL of deionized water) within a 100 mL Erlenmeyer flask. The nominal dopant concentrations were 1.0 mol% Tm^{3+} and 20.0 mol% Yb^{3+} (relative to the Y^{3+} content). Ammonium heptamolybdate was introduced separately to achieve the desired Mo^{6+} stoichiometry. The resulting mixture underwent magnetic stirring at 70–80 °C until complete dissolution was achieved, yielding a transparent solution. Citric acid was subsequently added at a molar ratio of 1.5 : 1 relative to the total metal cations, inducing a color transition from colorless to pale blue. The reaction vessel was maintained at 80 °C under continuous agitation to promote gel formation. After gelation, the product was dried at 150 °C for 12 hours, subjected to a preliminary heat treatment at 400 °C for 2 hours, ground to a fine powder using an agate mortar, and finally calcined at 600 °C for 4 hours in ambient air to yield the crystalline phosphor powder. The doping concentrations were selected based on the distinct roles of the lanthanide ions in the upconversion mechanism. Yb^{3+} acts as the sensitizer with a large absorption cross-section at 975 nm; a concentration of 10 mol% was chosen to ensure efficient pump light absorption and energy transfer to the activator ions without inducing significant concentration quenching. Tm^{3+} acts as the activator responsible for the visible and NIR emissions. A lower concentration of 1 mol% was selected to minimize cross-relaxation processes between Tm^{3+} ions, which typically lead to luminescence quenching at higher doping levels. These concentrations are consistent with optimal doping levels reported for Tm^{3+}/Yb^{3+} co-doped molybdate hosts in recent literature[2,27,32]

2.2. Characterization

X-ray diffraction measurements were performed using a Bruker D8 Advance diffractometer (Bruker AXS, Madison, WI, USA) equipped with Cu Kα radiation (λ = 1.5406 Å). Data collection parameters were set at 40 kV and 30 mA, with angular scans spanning 2θ = 5–80°. Structural analysis and phase identification were conducted through Rietveld refinement employing the FULLPROF software package to assess the crystallinity and structural integrity of the synthesized samples.

Particle morphology and dimensional distribution were characterized *via* field-emission scanning electron microscopy (FE-SEM, Hitachi TM3000, Hitachi High-Tech, Tokyo, Japan) and transmission electron microscopy (TEM, Hitachi HT7700, Hitachi High-Tech, Tokyo, Japan). Luminescence properties were investigated using a combination of two complementary detection systems. Upconversion, luminescence and near-infrared

emission spectra were acquired using an Andor Shamrock 500 spectrometer (Andor Technology, Belfast, UK) equipped with dual CCD detectors: a silicon CCD covering the 400–1000 nm region and an InGaAs CCD for the 900–1700 nm spectral window, with instrumental spectral response calibration applied to all measurements. Photoluminescence excitation was provided by a fiber-coupled continuous-wave laser diode operating at 975 nm with an output power of 150 mW and a focused spot diameter of approximately 0.2 mm. All temperature-dependent LIR measurements were performed under 975 nm excitation at 15 mW, focused with a 10 cm focal length lens, yielding a power density of 2.4 W cm^{-2} on the sample surface.

3. Structural properties and particle morphology

X-ray diffraction (XRD) analysis was performed to confirm the phase purity and crystal structure of the Tm^{3+}/Yb^{3+}-codoped NSYM phosphors. As shown in Fig. 1, the experimental XRD pattern of NSYM:Tm^{3+}/Yb^{3+} is in excellent agreement with the reference pattern of $NaSrY(MoO_4)_3$ (Joint Committee on Powder Diffraction Standards, JCPDS Card No. 70-0257),[33,34] with no detectable secondary phases. This confirms the formation of a monophasic material. All diffraction peaks were successfully indexed to the tetragonal crystal system with a space group of $I4_1/a$ (No. 88) following structural refinement. The observed diffraction profile closely resembles that of $NaLa(MoO_4)_2$-type compounds,[35] which share a related scheelite-derived tetragonal structure, further supporting the structural assignment. Rietveld refinement was employed to assess phase purity and refine the unit cell parameters, yielding $a = b = 5.26257$ Å, $c = 11.56482$ Å, and $\beta = 90^\circ$, as show in Fig. S1. Notably, the XRD patterns remained unchanged upon doping with Tm^{3+} and Yb^{3+}, indicating that these lanthanide ions are successfully incorporated into the Y^{3+} lattice sites without inducing significant structural distortion. This facile substitution is attributed to the similar ionic radii of the eight-coordinated (CN = 8) ions: Y^{3+} (0.900 Å), Yb^{3+} (0.950 Å), and Tm^{3+} (0.880 Å). The morphology and particle size of the synthesized NSYM:Tm^{3+}/Yb^{3+} phosphor were examined using a scanning electron microscope (SEM), as shown in Fig. 1; the micrographs reveal irregular, predominantly spherical nanoparticles that exhibit moderate agglomeration. The primary particle size is estimated to be approximately 200 nm, consistent with the nanoscale dimensions suitable for optical nanothermometry and bioimaging applications.

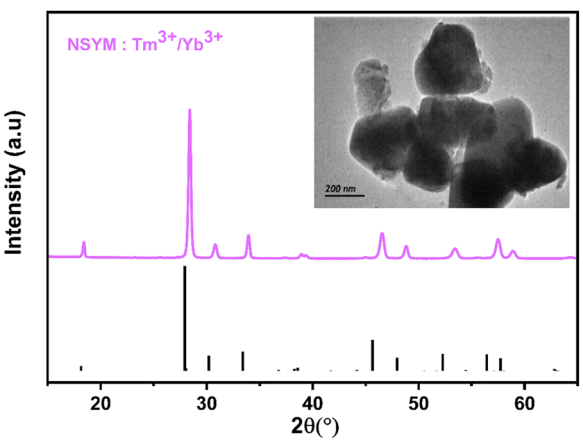

Fig. 1 XRD pattern of NSYM:Yb^{3+}/Tm^{3+} phosphor. Inset shows TEM image.

Under 975 nm excitation, NSYM:Tm^{3+}/Yb^{3+} exhibits rich multi-wavelength luminescence spanning the visible region to the NIR-III region, arising from both upconversion (UC) and down-conversion (DC) processes. Fig. 2 shows the photoluminescence emission spectrum, with visible UC emissions at 487 nm ($^1G_4 \rightarrow {}^3H_6$) and 693 nm ($^1G_4 \rightarrow {}^3F_4$), resulting from the sequential energy transfer from Yb^{3+} to Tm^{3+} and subsequent population of high-lying excited states. In contrast, the NIR emissions at 797 nm ($^3H_4 \rightarrow {}^3H_6$), 1450 nm ($^3H_4 \rightarrow {}^3F_4$), and 1625 nm ($^3F_4 \rightarrow {}^3H_6$) originate from down-conversion transitions, where lower-energy excited states relax radiatively without photon upconversion.[8,27,36] The 797 nm band falls within the first biological window (NIR-I, 650–950 nm). The 1450 nm emission represents an important spectral band, which often appears around 1400 nm in bioimaging applications, due to its reduced background interference, and the 1625 nm peak lies in the third biological window (NIR-III, 1500–1850 nm), a region valued for its deep tissue penetration, minimal scattering, and negligible autofluorescence.[28,34,37] The integrated presence of upconverted visible emission and down-converted near-infrared luminescence (NIR-I/III) within the same co-doped phosphor system offers significant practical advantages. The visible UC bands provide a basis for developing high-sensitivity ratiometric temperature sensors, whereas the near-infrared down-converted signals enable penetration into biological tissue and facilitate non-contact thermal characterization. This study represents, to our knowledge, the first comprehensive report of Tm^{3+} luminescence emission across the complete near-infrared spectrum (NIR-I and NIR-III windows) from the NSYM host matrix under 975 nm photoexcitation. These findings underscore the versatility of this material platform for biomedical photonics applications requiring multi-wavelength optical functionality.

The photon-number dependence of Tm^{3+} emissions provides key insight into the energy-transfer mechanisms underpinning the observed luminescence. To elucidate the UC, the dependence of emission intensity on excitation pump power was investigated. Theoretically, the integrated UC emission intensity (I) scales with the pump power (P) according to the relationship:[38,39]

$$I \approx P^n \quad (1)$$

where n represents the number of 975 nm photons required to populate the emitting state. A log–log plot of emission intensity *versus* pump power density thus yields n as the slope, revealing the dominant excitation mechanism.[40,41] As shown in Fig. 3(a), the slope for the blue UC emission ($^1G_4 \rightarrow {}^3H_6$ at 487 nm) is 2.28, indicating that approximately three photons are involved in populating the $^1G_4$ level consistent with a three-step energy

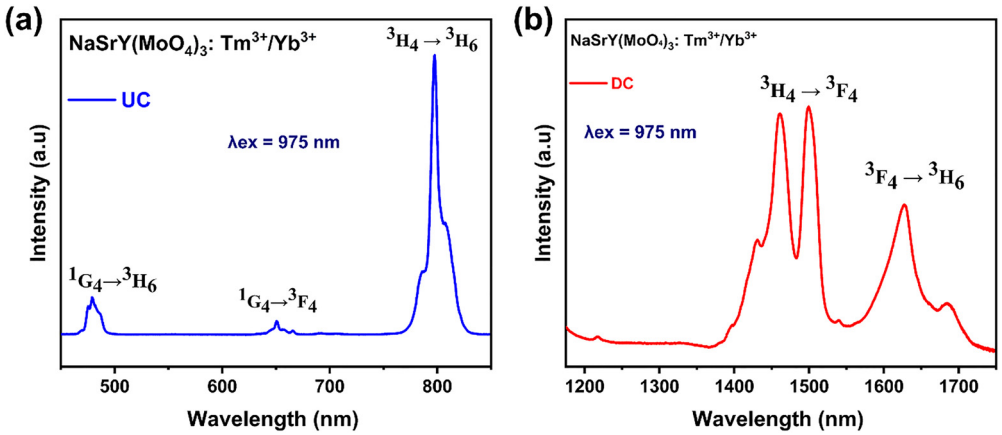

Fig. 2 (a) and (b): The up- and down-conversion luminescence spectra of NSYM:Tm^{3+}/Yb^{3+} under 975 nm laser excitation.

transfer upconversion (ETU) process mediated by Yb^{3+}. In contrast, the NIR emission at 797 nm ($^3H_4 \rightarrow {}^3H_6$) exhibits a slope of 1.62, signifying a two-photon process for populating the $^3H_4$ state.

The mechanisms of absorption, energy transfer, UC and DC can be clearly illustrated using the energy level diagram of Tm^{3+} and Yb^{3+} ions, as depicted in Fig. 3(b). The promotion of Tm^{3+} ions to higher excited states *via* a variety of excitation mechanisms, such as cooperative energy transfer (CET), energy transfer UC (ETU), and ground state absorption (GSA), is evident in this picture.

However, the Tm^{3+} energy level diagram makes it clear that three photons are needed to reach the $^1G_4$ level and two photons are needed to occupy the $^3H_4$ level, as shown in Fig. 3(b). Two consecutive energy transfers from Yb^{3+} ions stimulated to the $^2F_{5/2}$ state drive the UC process to the $^3H_4$ level.[42] In the ground state ($^3H_6$), an excited Yb^{3+} ion first non-resonantly transfers its energy to a Tm^{3+} ion, elevating it to the $^3H_5$ level before it relaxes to the $^3F_4$ level. The Tm^{3+} ion is then excited from $^3F_4$ to the $^3F_2$ or $^3F_3$ level (ET2) by a second excited Yb^{3+} ion, and then it relaxes non-radiatively to the $^3H_4$ level. A third energy transfer step (ET3) from an excited Yb^{3+} ion further excites the Tm^{3+} ion to the $^1G_4$ level, completing a three-photon upconversion process. This mechanism highlights the crucial role of Yb^{3+} ions as sensitizers, owing to their high absorption cross-section at 975 nm, which facilitates efficient energy transfer to Tm^{3+} ions.[43,44]

3.1. Optical temperature sensing

The lanthanide trivalent thulium ion (Tm^{3+}) presents exceptional versatility for wavelength-resolved temperature sensing owing to its intricate energy level structure and consequent emission spanning from the visible spectrum through the third near-infrared biological window (NIR-III). Although Tm^{3+}/Yb^{3+} co-doped systems have received considerable attention for upconversion photoluminescence studies, their utilization in ratiometric thermal sensing particularly with emphasis on NIR-III transitions has remained relatively unexploited. Conventional investigations predominantly emphasize visible or NIR-I luminescence channels, with minimal investigation into the thermal behavior of NIR-III bands. This work demonstrates that the NSYM host material doped with Tm^{3+}/Yb^{3+} enables multi-window thermal characterization with particular focus on the NIR-III spectral region.

Temperature-dependent photoluminescence spectra of NSYM: Tm^{3+}/Yb^{3+} nanocrystals were acquired under 975 nm photoexcitation across the 297–356 K thermal range (Fig. 4(a) and (b)).

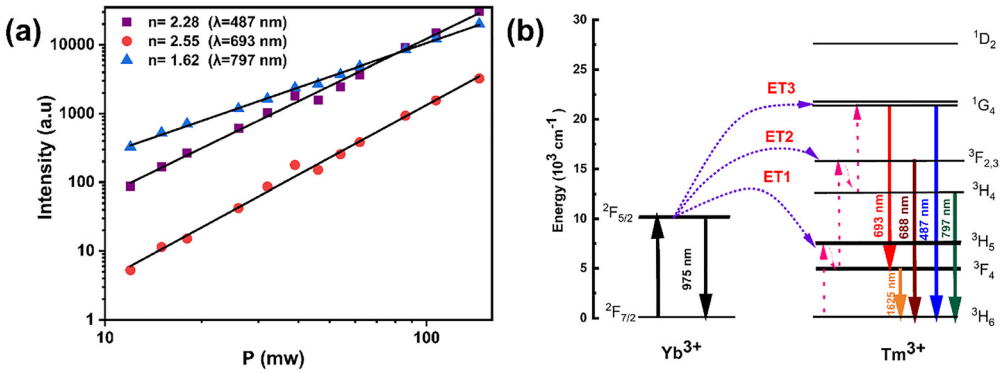

Fig. 3 (a) Dependence of the intensity on the pump power of NSYM:Tm^{3+}/Yb^{3+} and (b) partial energy level diagram of Yb^{3+} and Tm^{3+} ions showing the processes that occur when the NSYM:Tm^{3+}/Yb^{3+} phosphor is excited at 975 nm.

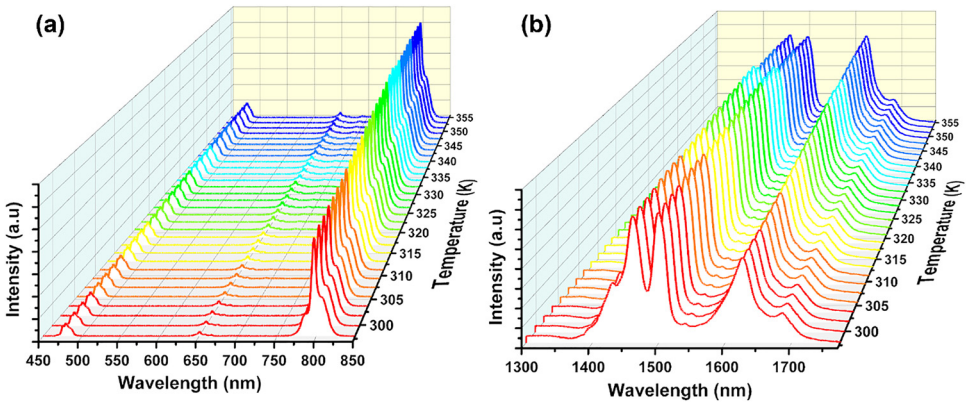

Fig. 4 Temperature-dependence of the emission spectra of the NSYM:Tm^{3+}/Yb^{3+} material: (a) upconversion and (b) down-conversion under excitation at 975 nm.

Increasing temperature elicits monotonic intensity diminishment in the visible UC bands ($^1G_4$ emission at 487 and 693 nm) and the $^3H_4$ transition (797 nm), a trend attributable to enhanced radiationless decay through multiphonon deexcitation pathways. Conversely, the near-infrared emission centered at 1625 nm ($^3F_4 \rightarrow {}^3H_6$ transition) displays a contrasting positive temperature coefficient. This anomalous response originates from thermally promoted cross-relaxation and phonon-mediated energy transfer mechanisms coupling the $^3H_4$ and $^3F_4$ excited states, with the latter achieving higher population efficiency at elevated temperatures. Thus, the $^3F_4$ manifold functions as a thermally responsive energy reservoir, rendering the 1625 nm emission particularly suited for NIR-III thermal measurement applications. A significant observation is the enhanced thermal stability of the visible UC luminescence relative to the near-infrared DC photoluminescence. This differential resilience to thermal quenching derives from the substantial energy separation between the $^1G_4$ level and underlying states, effectively attenuating multiphonon deexcitation processes. The distinct thermal sensitivities exhibited between visible and near-infrared emission channels establish a reliable basis for developing ratiometric temperature sensors with enhanced sensitivity and measurement precision.

Following confirmation of concurrent visible UC and near-infrared DC luminescence under 975 nm photoexcitation, the thermal sensing capabilities of NSYM:Tm^{3+}/Yb^{3+} were systematically evaluated. The pronounced temperature sensitivity of photoluminescence signals across the visible, NIR-I, and NIR-III spectral bands indicates feasibility for thermal monitoring across a physiologically relevant temperature window.

To characterize the temperature-sensing performance of NSYM:Tm^{3+}/Yb^{3+}, two complementary analytical methodologies were implemented: Boltzmann-based and non-Boltzmann-based luminescence intensity ratio (LIR) analyses, with selection guided by the electronic configuration of Tm^{3+}. Although Tm^{3+} does not possess the classical thermally coupled level (TCL) architecture conventionally described as paired excited states exhibiting 200–2000 cm^{-1} energy separation and Boltzmann-distributed population dynamics, certain emission transitions in this material system demonstrate empirically observed Boltzmann-type thermal response characteristics. These emission pairs consequently facilitate accurate ratiometric thermal quantification. For non-thermally coupled levels (NTCLs)—such as emission transitions originating from distinct excited states that do not share a common thermalizing manifold—the temperature dependence of the fluorescence intensity ratio (FIR) typically follows a modified empirical form, often expressed as:[27,45–47]

$$\mathrm{LIR_{NTCL}} = \frac{I_1}{I_2} = A + B \times \exp\left(\frac{-C}{K_B T}\right) \quad (2)$$

where I_1 and I_2 are integrated emission intensities, A is the constant that depends on the experimental setup (for LIR1 $A = 0$), K_B is the Boltzmann constant, T is absolute temperature, and ΔE represents an effective energy gap derived from the fit.

Fig. 5 shows the temperature-dependent LIR for the emission pairs (LIR1–LIR8) under 975 nm excitation. The integrated intensities were obtained by Gaussian fitting of each emission band to ensure accuracy.

In contrast, LIR1, LIR2, LIR3, and LIR4, as well as LIR5, LIR6, LIR7, and LIR8, which involve emissions from the same upper level, all follow the NTCL model eqn (2) with high fidelity ($R^2 > 0.99$), reflecting the temperature-dependent branching ratios between the radiative pathways.

However, when we compare them with wavelengths in the third biological window, we get a significant increase and the maximum of the LIR8(1625/1500) reaches 0.9. This indicates the importance of the 1625 nm peak to improve our results.

These results demonstrate that NSYM:Tm^{3+}/Yb^{3+} supports NTCL mode thermometry offering flexibility for multi-parameter thermal sensing across biological windows.

In order to investigate the performance of any nanothermometer, parameters such as absolute sensitivity and relative sensitivities should be determined. The absolute sensitivity (S_a) was calculated using eqn (3). This parameter is usually expressed in K^{-1}.[2,17,48]

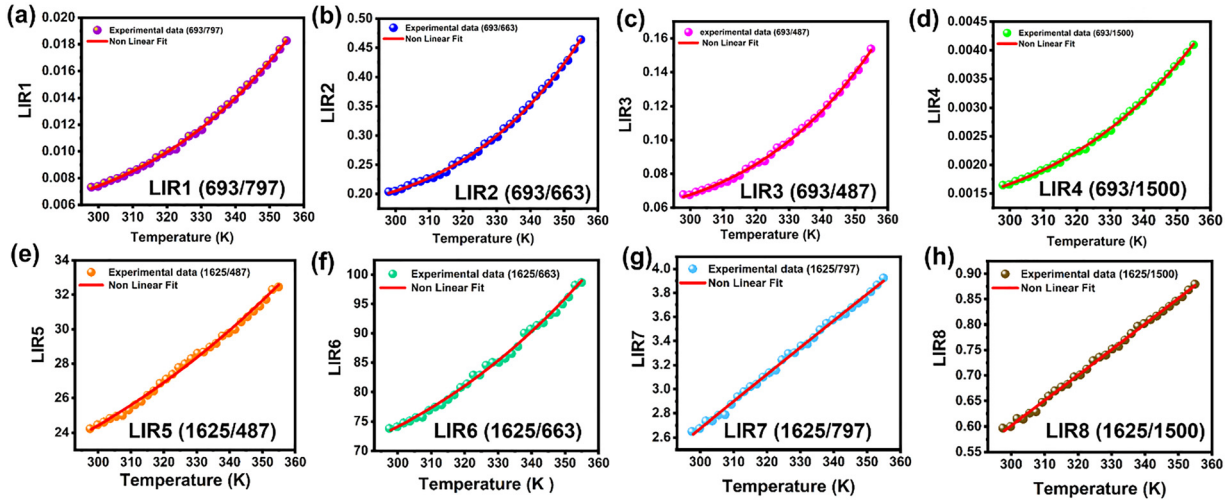

Fig. 5 Temperature-dependent luminescence intensity ratios (300–360 K). (a) LIR1 (693/797 nm), (b) LIR2 (693/663 nm), (c) LIR3 (693/487 nm), (d) LIR4 (693/1500 nm), (e) LIR5 (1625/487 nm), (f) LIR6 (1625/663 nm), (g) LIR7 (1625/797 nm), and (h) LIR8 (1625/1500 nm).

$$S_a = \frac{d\mathrm{LIR}}{dT} \quad (3)$$

The absolute sensitivity S_a provides critical insight into the thermal response of each emission pair. For LIR1 (693/797), LIR2 (693/663), LIR3 (693/487) and LIR4 (693/1500), it increases monotonically with temperature, with maximum values of 0.0028, 0.0088, 3.29×10^{-4}, and 7.47×10^{-5} K^{-1}, respectively. These trends reflect the underlying thermal activation of non-radiative pathways that modulate the branching ratios between competing emissions. Notably, LIR7 (1625/797) exhibits an atypical behavior: its absolute sensitivity decreases slightly from 0.0224 to 0.0220 K^{-1} over the measured range, likely due to saturation effects or competing relaxation mechanisms at higher temperatures.

However, the relative temperature sensitivity, S_r, allows the quantitative comparison of thermometers with different operating principles (developed using different measuring setups). This parameter reflects by what amount the analyzed thermometric parameter (LIR) changes per 1 K (typically expressed in % K^{-1}), and it is defined according to eqn (4).[49–52]

$$S_r = \frac{1}{\mathrm{LIR}} \times \frac{\delta \mathrm{LIR}}{\delta T} \times 100\% \quad (4)$$

Fig. 6 shows the temperature dependence of the relative sensitivity S_r for various LIRs in NSYM:Tm^{3+}/Yb^{3+}. As commonly observed in lanthanide-based thermometers, the relative sensitivity decreases with increasing temperature for certain emission pairs (*e.g.*, LIR7 and LIR8). In contrast, the LIR2 and LIR3 ratios exhibit a monotonic increase with temperature, reaching maximum values of 1.90% K^{-1} and 1.80% K^{-1}, respectively, near 356 K. These high sensitivities in the visible range are particularly advantageous for optical thermometry, as they benefit from a favorable balance between moderate tissue

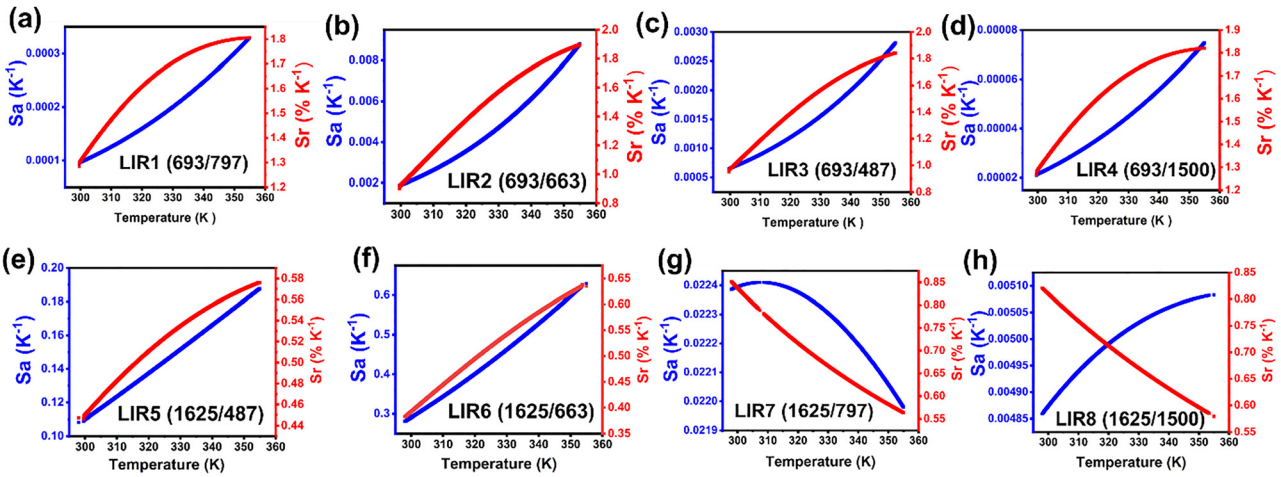

Fig. 6 Absolute sensitivity S_a and relative sensitivity S_r variations obtained from the temperature-dependent luminescence intensity ratios of the NSYM:Tm^{3+}/Yb^{3+} phosphor (a) LIR1 (693/797 nm), (b) LIR2 (693/663 nm), (c) LIR3 (693/487 nm), (d) LIR4 (693/1500 nm), (e) LIR5 (1625/487 nm), (f) LIR6 (1625/663 nm), (g) LIR7 (1625/797 nm), and (h) LIR8 (1625/1500 nm).

absorption and sufficient penetration depth for superficial bioimaging applications. Notably, while most reported lanthanide thermometers operate within a single biological window, our Tm^{3+}/Yb^{3+}-doped NSYM phosphor demonstrates measurable relative sensitivity across the most important biological transparency windows: NIR-I (~797 nm, $^3H_4 \rightarrow {}^3H_6$) and NIR-III (1625 nm, $^3F_4 \rightarrow {}^3H_6$). (Do not forget the significance of the peak near 1450 nm, as it is almost within the range of the second biological window: $^3H_4 \rightarrow {}^3F_4$.) Although the sensitivity in the NIR-III window is lower than that in the visible region, it remains significant: for the 1625/1500 nm ratio (assigned to $^3F_4 \rightarrow {}^3H_6/{}^3H_4 \rightarrow {}^3F_6$), S_r reaches 0.82% K^{-1} a value that substantially exceeds that of Er^{3+}-based systems. For instance, under comparable conditions, Er^{3+}:$NaYF_4$ exhibits only 0.14% K^{-1} in the NIR-III window (1512/1540 nm).[53] In the following table, we present a summary of the values for S_r. The demonstrated performance characteristics highlight the distinctive advantages of Tm^{3+} as a thermal sensing agent for subsurface biological imaging, leveraging its extensive cascade of near-infrared transitions and efficient energy transfer from Yb^{3+} sensitizer ions. Comprehensive evaluation of both relative and absolute thermal sensitivity metrics across the three tissue-transparent spectral windows illuminates the photophysical behavior of the Tm^{3+}/Yb^{3+}-modified NSYM lattice and delineates foundational design criteria for developing advanced optical nanothermometers optimized toward clinical and biomedical deployment. Despite inherent limitations including radiative losses from small energy splittings within the Tm^{3+} manifold, modest photoluminescence quantum efficiency in the NIR-III spectral region, and competing upconversion and cross-relaxation deexcitation channels, the NSYM:Tm^{3+}/Yb^{3+} composition demonstrates outstanding thermal responsiveness, an extended operational temperature window (297–356 K), and consistent luminescence output spanning the NIR-I and NIR-III regions. A critical advantage is the material's functionality at reduced excitation irradiance levels, maintaining biological safety thresholds while generating sufficient signal intensity in penetration-optimized spectral domains that concurrently suppress endogenous biological luminescence (Table 1).

Comparative analysis presented in Table 2 documents superior performance relative to previously reported Tm^{3+}-based thermal sensors regarding both thermal responsivity and multi-spectral functionality. The optimal luminescence intensity ratio pairs (693/663 nm), (693/1500 nm), and (1625/1500 nm) yield maximum relative sensitivities of 1.90% K^{-1}, 0.82% K^{-1}, and 0.82% K^{-1}, respectively, throughout the physiologically applicable thermal range. While outstanding challenges persist, such as amplification of NIR-III luminescence intensity, suppression of thermally induced emission losses at higher temperatures, and implementation compatibility within heterogeneous *in vivo* tissue environments, this investigation constitutes a significant milestone toward realizing practical, multi-window optical nanothermometers capable of delivering non-invasive, high-accuracy thermal measurements in living biological systems.

Table 1 Luminescence intensity ratio (LIR), spectral window, and maximum sensitivity (S_r) in % K^{-1}

LIR	Ratio (nm)	Spectral window	$S_{r(max)}$ (% K^{-1})
LIR1	693/797	Visible/NIR-I	1.40
LIR2	693/663	Visible	1.90
LIR3	693/487	Visible/Visible	1.80
LIR4	693/1500	Visible/NIR-III	1.82
LIR5	1625/487	Visible/NIR-III	0.57
LIR6	1625/663	Visible/NIR-III	0.63
LIR7	1625/797	NIR-III/NIR-I	0.85
LIR8	1625/1500	NIR-III	0.82

In addition to absolute (S_a) and relative (S_r) sensitivities, the temperature resolution (δT) is a critical figure of merit that defines the smallest detectable temperature change. It is expressed as[59–61]

$$\delta T = \frac{1}{S_r} \times \frac{\delta \mathrm{LIR}}{\mathrm{LIR}} \quad (5)$$

where $\frac{\delta \mathrm{LIR}}{\mathrm{LIR}}$ represents the relative uncertainty in the luminescence intensity ratio (LIR) measurement, and S_r is the relative thermal sensitivity. The value thus depends not only on the intrinsic thermometric performance of the material (*i.e.*, S_r) but also on experimental factors such as the signal-to-noise ratio (SNR), detector sensitivity, and calibration stability. To improve temperature resolution, data acquisition quality can be enhanced, for instance, by increasing the integration time or averaging multiple measurements to suppress random noise and minimize measurement uncertainty Using (eqn (5)), we calculated the theoretical temperature resolution for NSYM:Tm^{3+}/Yb^{3+} across the 297–356 K range (Fig. 7). Remarkably, all LIR-based thermometers in this system achieve $\delta T < 1$ K, with the best-performing pairs (*e.g.*, 693/663 nm) reaching as low as 0.4–0.5 K. Such high resolution combined with multi-window operation and low excitation power underscores the strong potential of this material for precision thermal sensing in biological environments, where sub-kelvin accuracy is often required.

These results confirm that both non-thermally compensated luminescence (NTCL) and quasi-thermally compensated luminescence (quasi-TCL) based luminescence intensity ratio (LIR) thermometry strategies exhibit high precision across the entire 297–356 K range, with temperature resolution (δT) consistently below 1 K. This level of performance provides a reliable estimate of the thermal resolution achievable with NSYM:Tm^{3+}/Yb^{3+} in practical sensing scenarios. To quantify the experimental temperature uncertainty (*i.e.*, the limit of detection), we performed 100 repeated LIR measurements at room temperature (297 K) under identical experimental conditions. The resulting distributions (Fig. S2) were fitted with Gaussian functions, and standard deviation (σ) was used to determine the uncertainty in LIR (δLIR). The full width at half-maximum (FWHM) of each peak corresponds to the experimental resolution of the sensor, with values plotted in Fig. S3. These measurements confirm that the temperature uncertainty remains as low as 0.4–0.5 K, validating the high reproducibility and reliability of the NSYM:Tm^{3+}/Yb^{3+} system. Collectively, these findings establish NSYM-based upconverting phosphors as high-performance

Table 2 Maximum relative thermal sensitivity $S_{r(max)}$ of Tm^{3+}-doped luminescent materials in biological windows

Samples	λ_{ex} (nm)	λ_{em} (nm)	$S_{r(max)}$ (% K^{-1})	Biological windows	Ref.
$NaSrY(Mo_4)_3:Er^{3+}/Ho^{3+}/Yb^{3+}$	975	(1512/1540)	0.14	NIR-III	54
$NaSrY(MoO_4)_3:Er^{3+}/Ho^{3+}/Yb^{3+}$	975	(525/660)	1.2	Visible	54
$Ba_3GdV_3O_{11}:Er^{3+}/Tm^{3+}/Yb^{3+}$	975	(700/650)	1.4	NIR-I	40
$La_2Mo_3O_{12}:Tm^{3+}/Yb^{3+}$	975	702/652	7.37	NIR-I	55
$Cs_2NaLuCl_6:Mn^{2+}$	320	STE/Mn^{2+}	1.02	Visible	56
$Y_2Mo_4O_{15}:Tm^{3+}/Er^{3+}$	975	(700/650)	1.3	NIR-I	57
$LiYbF_4:Er@LiYF_4:Er^{3+}$	980	(1425/1650)	0.248	NIR-III	58
$NaSrY(Mo_4)_3:Tm^{3+}/Yb^{3+}$	975	(693/663)	1.9	Visible	This work
$NaSrY(Mo_4)_3:Tm^{3+}/Yb^{3+}$	975	(1625/1500)	0.82	NIR-III	This work

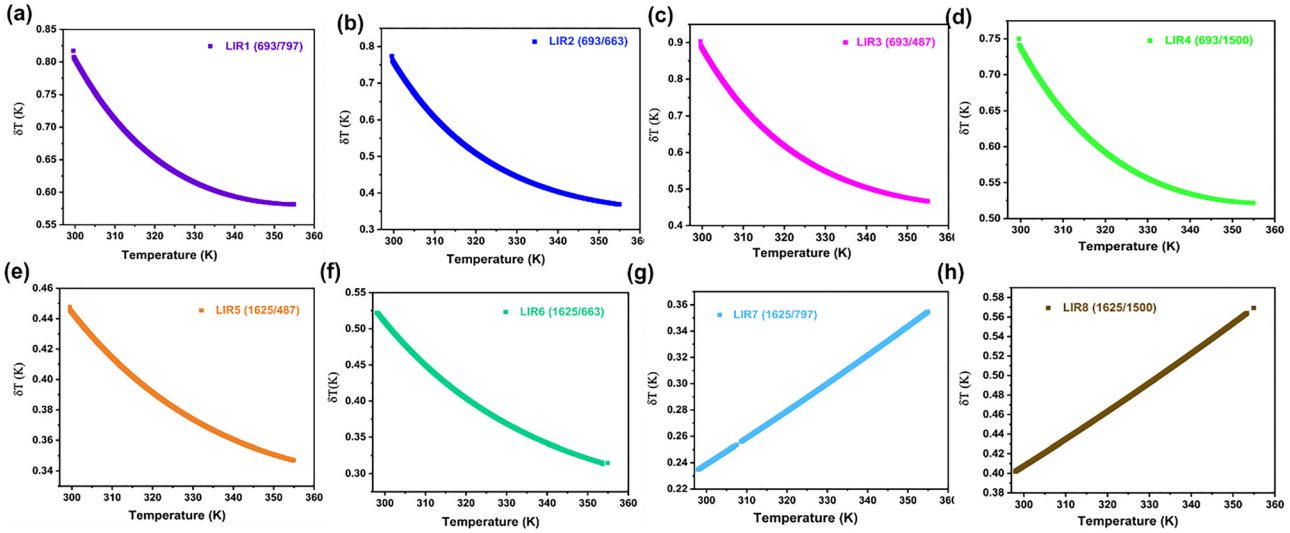

Fig. 7 Temperature uncertainty values δT of NSYM:Tm^{3+}/Yb^{3+} obtained for (a) (693/797), (b) (693/663), (c) (693/487), (d) (693/1500), (e) (1625/487), (f) (1625/663), (g) (1625/797) and (h) (1625/1500).

optical thermometers with exceptional sensitivity, sub-kelvin resolution, and minimal measurement error, making them highly suitable for precision thermal sensing in both biological and industrial applications.

4. Conclusion

In summary, Tm^{3+}/Yb^{3+} co-doped $NaSrY(MoO_4)_3$ (NSYM) phosphors were successfully synthesized *via* a sol–gel method. The materials exhibit simultaneous luminescence across the visible, NIR-I, and NIR-II biological windows under low-power excitation, offering a biocompatible platform for multifunctional theranostics and non-invasive temperature sensing. The materials demonstrate exceptional ratiometric thermometric performance, with a maximum relative thermal sensitivity of 1.90% K^{-1} over the physiologically relevant temperature range of 297–356 K in the visible range. The observed temperature-dependent luminescence arises from the synergy of down-conversion processes, wherein temperature-activated cross-relaxation selectively populates the $^3F_4$ level, thereby enabling highly sensitive NIR-III thermometry (S_r = 0.82% K^{-1} for the 1625/1500 nm ratio). Combined with its high sensitivity, sub-kelvin resolution (0.4–0.5 K), and broad operational range (297–356 K), NSYM:Tm^{3+}/Yb^{3+} represents a highly promising platform for non-invasive optical thermometry in biomedical diagnostics, photothermal therapy monitoring, and industrial thermal sensing applications. This work thus establishes a robust foundation for the rational design of next-generation multi-window luminescent nanothermometers based on tailored rare-earth-doped molybdate hosts.

Conflicts of interest

There are no conflicts to declare.

Data availability

The data supporting this article have been included in the article file and supplementary information (SI). Supplementary information is available. See DOI: https://doi.org/10.1039/d6ma00173d.

References

1 M. Back, E. Trave, J. Ueda and S. Tanabe, Ratiometric Optical Thermometer Based on Dual Near-Infrared Emission in Cr^{3+}-Doped Bismuth-Based Gallate Host, *Chem.*

Mater., 2016, **28**(22), 8347–8356, DOI: 10.1021/acs.chemmater.6b03625.

2 I. Kachou, K. Saidi, Z. E. A. A. Taleb, C. Hernández-Álvarez, M. Dammak and I. R. Martín, Dual-Functional Tm^{3+}/Yb^{3+}-Doped $LiCaLa(MoO_4)_3$ Phosphors: High-Sensitivity Thermal Sensing and Deep-Tissue NIR Bio-Imaging, *Mater. Adv.*, 2025, **6**(16), 5546–5557, DOI: 10.1039/D5MA00489F.

3 A. Soleilhac, Thermographie Multi-Échelle Par Méthodes Optiques Sur Gouttelettes et Bulles Micrométriques: Applications Aux Nanoparticules Irradiées Par Laser Ultra-Intense et Aux Édifices Biomoléculaires En Cours de Déshydratation. Theses, Université de Lyon, 2017. https://theses.hal.science/tel-01688828 (accessed 2025-10-28).

4 K. Saidi, I. Kachou, K. Soler-Carracedo, M. Dammak and I. R. Martín, $Ba_2YV_3O_{11}$ Er^{3+}/Yb^{3+} Nanostructures for Temperature Sensing in the Presence of Bismuth Ions, *ACS Appl. Nano Mater.*, 2023, **6**, 12345–12356, DOI: 10.1021/acsanm.3c02911.

5 F. Ayachi, K. Saidi, M. Dammak, W. Chaabani, I. Mediavilla-Martínez and J. Jiménez, Dual-Mode Luminescence of Er^{3+}/Yb^{3+} Codoped $LnP_{0.5}V_{0.5}O_4$ (Ln = Y, Gd, La) for Highly Sensitive Optical Nanothermometry, *Mater. Today Chem.*, 2023, **27**, 101352, DOI: 10.1016/j.mtchem.2022.101352.

6 L. Peng, F. Qin, C. Wang, L. Li and Z. Zhang, A High-Precision Thermometry Strategy by Replacing the Infrared with Visible Light for Detection, *Opt. Lett.*, 2023, **48**(15), 4061–4064, DOI: 10.1364/OL.494971.

7 K. Pushpendra, R. Kunchala, R. Kalia and B. S. Naidu, Excitation Dependent Visible and NIR Photoluminescence Properties of Er^{3+}, Yb^{3+} Co-Doped $NaBi(MoO_4)_2$ Nanomaterials, *RSC Adv.*, 2020, **10**(25), 14525–14530, DOI: 10.1039/D0RA01272F.

8 M. Fhoula, I. Kachou, K. Saidi, M. Dammak, I. Mediavilla and J. Jiménez, High-Sensitivity Dual-Mode Nanothermometry in Novel $Gd_2Mo_4O_{15}$:$Er^{3+}/Tm^{3+}/Yb^{3+}$ Phosphors, *Ceram. Int.*, 2025, **51**(26, Part C), 50694–50702, DOI: 10.1016/j.ceramint.2025.08.297.

9 K. Soler-Carracedo, I. R. Martín, F. Lahoz, H. C. Vasconcelos, A. D. Lozano-Gorrín, L. L. Martín and F. Paz-Buclatin, Er^{3+}/Ho^{3+} Codoped Nanogarnet as an Optical FIR Based Thermometer for a Wide Range of High and Low Temperatures, *J. Alloys Compd.*, 2020, **847**, 156541, DOI: 10.1016/j.jallcom.2020.156541.

10 I. Vallerini Barbosa, Luminescent Oxide Nanocrystals for the Development of in Vivo Thermal Sensors. Theses, Université Grenoble Alpes [2020-...]; Universidade federal de Goiás, 2023. https://theses.hal.science/tel-04850264 (accessed 2025-10-28).

11 N. Jurga, M. Runowski and T. Grzyb, Lanthanide-Based Nanothermometers for Bioapplications: Excitation and Temperature Sensing in Optical Transparency Windows, *J. Mater. Chem. C*, 2024, **12**(32), 12218–12248.

12 M. Runowski, N. Stopikowska, D. Szeremeta, S. Goderski, M. Skwierczyńska and S. Lis, Upconverting Lanthanide Fluoride Core@Shell Nanorods for Luminescent Thermometry in the First and Second Biological Windows: β-$NaYF_4$:Yb^{3+}–Er^{3+}@SiO_2 Temperature Sensor, *ACS Appl. Mater. Interfaces*, 2019, **11**(14), 13389–13396, DOI: 10.1021/acsami.9b00445.

13 A. Nexha, J. J. Carvajal, M. C. Pujol, F. Díaz and M. Aguiló, Lanthanide Doped Luminescence Nanothermometers in the Biological Windows: Strategies and Applications, *Nanoscale*, 2021, **13**(17), 7913–7987, DOI: 10.1039/D0NR09150B.

14 S. Bi, Z. Deng, J. Huang, X. Wen and S. Zeng, NIR-II Responsive Upconversion Nanoprobe with Simultaneously Enhanced Single-Band Red Luminescence and Phase/Size Control for Bioimaging and Photodynamic Therapy, *Adv. Mater.*, 2023, **35**(7), 2207038, DOI: 10.1002/adma.202207038.

15 M. Kamimura, T. Matsumoto, S. Suyari, M. Umezawa and K. Soga, Ratiometric Near-Infrared Fluorescence Nanothermometry in the OTN-NIR (NIR II/III) Biological Window Based on Rare-Earth Doped β-$NaYF_4$ Nanoparticles, *J. Mater. Chem. B*, 2017, **5**(10), 1917–1925, DOI: 10.1039/C7TB00070G.

16 T. Grzyb, P. Kamiński, D. Przybylska, A. Tymiński, F. Sanz-Rodríguez and P. Haro Gonzalez, Manipulation of Up-Conversion Emission in $NaYF_4$ Core@shell Nanoparticles Doped by Er^{3+}, Tm^{3+}, or Yb^{3+} Ions by Excitation Wavelength—Three Ions—Plenty of Possibilities, *Nanoscale*, 2021, **13**(15), 7322–7333, DOI: 10.1039/D0NR07136F.

17 D. Jaque and F. Vetrone, Luminescence Nanothermometry, *Nanoscale*, 2012, **4**(15), 4301–4326, DOI: 10.1039/C2NR30764B.

18 C. D. S. Brites, X. Xie, M. L. Debasu, X. Qin, R. Chen, W. Huang, J. Rocha, X. Liu and L. D. Carlos, Instantaneous Ballistic Velocity of Suspended Brownian Nanocrystals Measured by Upconversion Nanothermometry, *Nat. Nanotechnol.*, 2016, **11**(10), 851–856, DOI: 10.1038/nnano.2016.111.

19 M. Runowski, S. Goderski, D. Przybylska, T. Grzyb, S. Lis and I. R. Martín, Sr_2LuF_7:Yb^{3+}–Ho^{3+}–Er^{3+} Upconverting Nanoparticles as Luminescent Thermometers in the First, Second, and Third Biological Windows, *ACS Appl. Nano Mater.*, 2020, **3**(7), 6406–6415, DOI: 10.1021/acsanm.0c00839.

20 Z. Li, K. Li, M. Dai, J. Zhao, D. Guo, G. Liang, Y. Wei and Z. Fu, Precision Design of Highly Sensitive Luminescent Thermometers *via* Crystal Field Splitting Engineering, *J. Colloid Interface Sci.*, 2025, **700**, 138380, DOI: 10.1016/j.jcis.2025.138380.

21 K. Saidi, M. Dammak, K. Soler-Carracedo and I. R. Martín, A Novel Optical Thermometry Strategy Based on Emission of Tm^{3+}/Yb^{3+} Codoped $Na_3GdV_2O_8$ Phosphors, *Dalton Trans.*, 2022, **51**(13), 5108–5117, DOI: 10.1039/D1DT03747A.

22 Y. Yu, Y. D. Zheng, F. Qin, Z. M. Cheng, C. B. Zheng, Z. G. Zhang and W. W. Cao, Experimental Investigation on the Upconversion Mechanism of 754nm NIR Luminescence of Ho^{3+}/Yb^{3+}:Y_2O_3, Gd_2O_3 under 976nm Diode Laser-excitation, *J. Lumin.*, 2011, **131**(2), 190–193, DOI: 10.1016/j.jlumin.2010.09.033.

23 X. Wang, Z. Chen, J. Zhang, S. Pan and J. Pan, Growth and Temperature-Dependent Spectral Properties of Yb^{3+}, Tm^{3+}

Co-Doped NaY $(MoO_4)_2$ Crystal, *Spectroscopy*, 2022, **37**, 16–24, DOI: 10.56530/spectroscopy.xq4572z5.

24 A. Zhang, Z. Sun, M. Jia, G. Liu, F. Lin and Z. Fu, Simultaneous Luminescence in I, II and III Biological Windows Realized by Using the Energy Transfer of $Yb^{3+} \rightarrow Er^{3+}/Ho^{3+} \rightarrow Cr^{3+}$, *Chem. Eng. J.*, 2019, **365**, 400–404, DOI: 10.1016/j.cej.2019.02.061.

25 G. Chen, S. Li, L. Zhang, X. Tan, W. Deng, M. He, M. Xu, Y. Yang, S. Zhang and Y. Hang, Growth and Spectra of Tm^{3+} Doped LuYO3 Single Crystal for 2 Mm Lasers, *Infrared Phys. Technol.*, 2020, **109**, 103431, DOI: 10.1016/j.infrared.2020.103431.

26 S. Chen, W. Song, J. Cao, F. Hu and H. Guo, Highly Sensitive Optical Thermometer Based on FIR Technique of Transparent NaY2F7:Tm^{3+}/Yb^{3+} Glass Ceramic, *J. Alloys Compd.*, 2020, **825**, 154011, DOI: 10.1016/j.jallcom.2020.154011.

27 X. Bai, D. Li, Q. Liu, B. Dong, S. Xu and H. Song, Concentration-Controlled Emission in LaF3:Yb^{3+}/Tm^{3+} Nanocrystals: Switching from UV to NIR Regions, *J. Mater. Chem.*, 2012, **22**(47), 24698, DOI: 10.1039/c2jm35403a.

28 D. Guo, H. Suo, J. Zhao, K. Li, Y. Zhang, R. Lu and Z. Fu, Brightening Full-Spectrum Lanthanide Mechanoluminescence in a Wurtzite Semiconductor *via* Structural Reconstruction, *Laser Photonics Rev.*, 2025, e02712, DOI: 10.1002/lpor.202502712.

29 H. Peng, M. I. J. Stich, J. Yu, L. Sun, L. H. Fischer and O. S. Wolfbeis, Luminescent Europium(III) Nanoparticles for Sensing and Imaging of Temperature in the Physiological Range, *Adv. Mater.*, 2010, **22**(6), 716–719, DOI: 10.1002/adma.200901614.

30 P. Woźny, K. Soler-Carracedo, N. Stopikowska, I. R. Martín and M. Runowski, Structure-Dependent Luminescence of Eu^{3+}-Doped Strontium Vanadates Synthesized with Different V: Sr Ratios – Application in WLEDs and Ultra-Sensitive Optical Thermometry, *J. Mater. Chem. C*, 2023, **11**(14), 4792–4807, DOI: 10.1039/D2TC05341A.

31 T. Zheng, M. Runowski, P. Woźny, B. Barszcz, S. Lis, M. Vega, J. Llanos, K. Soler-Carracedo and I. R. Martín, Boltzmann vs. Non-Boltzmann (Non-Linear) Thermometry - Yb^{3+}–Er^{3+} Activated Dual-Mode Thermometer and Phase Transition Sensor *via* Second Harmonic Generation, *J. Alloys Compd.*, 2022, **906**, 164329, DOI: 10.1016/j.jallcom.2022.164329.

32 Y. Bahrouni, I. Kachou, K. Saidi, C. Hernández-Álvarez, M. Dammak and I. R. Martin, Multifunctional Tm^{3+}/Yb^{3+}:$Na_5Y(MoO_4)_4$ Nanocrystals for Simultaneous Luminescent Nanothermometry, Photothermal Therapy and Deep Bioimaging in the NIR-I Window, *RSC Adv.*, 2026, **16**(5), 4452–4460, DOI: 10.1039/D5RA08947F.

33 M. Rajendran and S. Vaidyanathan, High Performance Red/Deep-Red Emitting Phosphors for White LEDs, *New J. Chem.*, 2020, **44**(14), 5354–5365, DOI: 10.1039/D0NJ00086H.

34 A. Shandilya, R. S. Yadav, A. K. Gupta and K. Sreenivas, Temperature-Dependent Light Upconversion and Thermometric Properties of Er^{3+}/Yb^{3+}-Codoped SrMoO4 Sintered Ceramics, *J. Mater. Sci.*, 2021, **56**(22), 12716–12731, DOI: 10.1007/s10853-021-06078-8.

35 P. Zhang, X. Wang, S. Zhao, X. Wang, R. Lei, L. Huang and S. Xu, An Integrated Temperature-Feedback Photothermal Therapy Platform Based on Dual-Functional Rare Earth-Doped $NaSrGd(MoO_4)_3$ Phosphors, *J. Phys. Chem. C*, 2023, **127**(26), 12770–12778, DOI: 10.1021/acs.jpcc.3c02449.

36 N.-N. Dong, M. Pedroni, F. Piccinelli, G. Conti, A. Sbarbati, J. E. Ramírez-Hernández, L. M. Maestro, M. C. Iglesias-de la Cruz, F. Sanz-Rodriguez, A. Juarranz, F. Chen, F. Vetrone, J. A. Capobianco, J. G. Solé, M. Bettinelli, D. Jaque and A. Speghini, NIR-to-NIR Two-Photon Excited CaF_2:Tm^{3+},Yb^{3+} Nanoparticles: Multifunctional Nanoprobes for Highly Penetrating Fluorescence Bio-Imaging, *ACS Nano*, 2011, **5**(11), 8665–8671, DOI: 10.1021/nn202490m.

37 G. Chen, H. Qiu, P. N. Prasad and X. Chen, Upconversion Nanoparticles: Design, Nanochemistry, and Applications in Theranostics, *Chem. Rev.*, 2014, **114**(10), 5161–5214, DOI: 10.1021/cr400425h.

38 H. Dong, L.-D. Sun and C.-H. Yan, Energy Transfer in Lanthanide Upconversion Studies for Extended Optical Applications, *Chem. Soc. Rev.*, 2015, **44**(6), 1608–1634, DOI: 10.1039/C4CS00188E.

39 P. V. dos Santos, M. T. de Araujo, A. S. Gouveia-Neto, J. A. Medeiros Neto and A. S. B. Sombra, Optical Temperature Sensing Using Upconversion Fluorescence Emission in Er^{3+}/Yb^{3+}-Codoped Chalcogenide Glass, *Appl. Phys. Lett.*, 1998, **73**(5), 578–580, DOI: 10.1063/1.121861.

40 I. Kachou, K. Saidi, C. Hernández-Álvarez, M. Dammak, R. Martín and I. Enhancing Thermometric Precision, Modulating the Temperature of Maximum Sensitivity *via* Erbium Dopant Addition in $Ba_2GdV_3O_{11}$:Tm^{3+}/Yb^{3+} Nano Phosphors, *Mater. Adv.*, 2024, **5**(20), 8280–8293, DOI: 10.1039/D4MA00699B.

41 H. Lv, P. Du, W. Li and L. Luo, Tailoring of Upconversion Emission in Tm^{3+}/Yb^{3+}-Codoped Y2Mo3O12 Submicron Particles *Via* Thermal Stimulation Engineering for Non-Invasive Thermometry, *ACS Sustainable Chem. Eng.*, 2022, **10**(7), 2450–2460, DOI: 10.1021/acssuschemeng.1c07323.

42 L. P. Ravaro, M. S. Arai, L. J. Q. Maia, M. Reza Dousti, P. H. D. O. Santiago, J. Ellena and A. S. S. De Camargo, Multifunctional Platform Based on a Copper(I) Complex and $NaYF_4$:Tm^{3+},Yb^{3+} Upconverting Nanoparticles Immobilized into a Polystyrene Matrix: Downshifting and Upconversion Oxygen Sensing, *ACS Appl. Mater. Interfaces*, 2022, **14**(42), 47902–47912, DOI: 10.1021/acsami.2c14579.

43 X. Wu, S. Zhan, G. Nie and Y. Liu, Ultrastrong Infrared Emission at 1460 Nm from Lanthanide-Doped Nanoparticles with Interfacial Sensitization, *Inorg. Chem.*, 2024, **63**(1), 760–765, DOI: 10.1021/acs.inorgchem.3c03756.

44 C. Hernández-Álvarez, G. Brito-Santos, R. Martín, I. Sanchiz, J. Saidi, K. Soler-Carracedo, K. Marciniak and M. Runowski, Multifunctional Optical Sensing Platform of Temperature, Pressure (Vacuum) and Laser Power Density: $NaYF_4$: Gd^{3+}, Yb^{3+}, Er^{3+} Nanomaterial as Luminescent Thermometer, Manometer and Power Meter, *J. Mater. Chem. C*, 2023, **11**(30), 10221–10229, DOI: 10.1039/D3TC01712E.

45 N. B. Amar, K. Saidi, C. Hernández-Álvarez, M. Dammak and I. R. Martin, Ultra-High-Sensitive Temperature Sensing Based on Emission Pr^{3+} and Yb^{3+} Codoped $Y_2Mo_3O_{12}$ Nanostructures, *Mater. Adv.*, 2025, **6**(2), 827–838, DOI: 10.1039/D4MA00746H.

46 Y. Zhang, P. Wang, H. Wang, X. Zheng, Y. Guo, N. Zhang and H. Liu, Visible and Near-Infrared Luminescence Properties of Nd^{3+}/Yb^{3+} Co-Doped Gd_2O_3 Phosphors for Highly Sensitive Optical Thermometry, *Dalton Trans.*, 2022, **51**(27), 10612–10622, DOI: 10.1039/D2DT01271E.

47 R. Yun, J. He, L. Luo, X. Liu, Z. Nie, W. Zhao and H. Wen, Upconversion Luminescence and Temperature Sensing Properties in $LiGd(WO_4)_2$:Er^{3+}, Yb^{3+}, Nd^{3+} Microparticles under 785 Nm Excitation, *Ceram. Int.*, 2021, **47**(11), 16062–16069, DOI: 10.1016/j.ceramint.2021.02.180.

48 M. Back, J. Ueda, H. Nambu, M. Fujita, A. Yamamoto, H. Yoshida, H. Tanaka, M. G. Brik and S. Tanabe, Boltzmann Thermometry in Cr^{3+}-Doped Ga_2O_3 Polymorphs: The Structure Matters!, *Adv. Opt. Mater.*, 2021, **9**(9), 2100033, DOI: 10.1002/adom.202100033.

49 X. Lai, P. Woźny, M. Runowski, L. Luo and P. Du, Regulating the Upconversion Luminescence Properties of Tm^{3+}/Yb^{3+}-Codoped $ZrScW_2PO_{12}$ Microparticles with a Negative Thermal Expansion Effect through Thermal Stimulation for Optical Thermometry, *Dalton Trans.*, 2024, **53**(10), 4607–4616, DOI: 10.1039/D3DT04110G.

50 C. D. S. Brites, R. Marin, M. Suta, A. N. Carneiro Neto, E. Ximendes, D. Jaque and L. D. Carlos, Spotlight on Luminescence Thermometry: Basics, Challenges, and Cutting-Edge Applications, *Adv. Mater.*, 2023, **35**(36), 2302749, DOI: 10.1002/adma.202302749.

51 Z. E. A. A. Taleb, I. Kachou, K. Saidi, M. Dammak, I. Mediavilla and J. Jiménez, Advanced Dual-Mode Er^{3+}/Yb^{3+} Phosphors for High-Precision Optical Thermometry across Broad Temperature Ranges, *Mater. Adv.*, 2025, **6**(7), 2385–2396, DOI: 10.1039/D5MA00108K.

52 X. Lai, W. Li, L. Luo and P. Du, Multi-Dimensional Tailoring of the Thermometric Behaviors of Er^{3+}/Yb^{3+}-Codoped $Y_2W_3O_{12}$ Polychromatic Upconverting Microparticles for Multi-Mode Visual Optical Thermometry, *J. Alloys Compd.*, 2024, **976**, 173311, DOI: 10.1016/j.jallcom.2023.173311.

53 Y. Wu, F. Li, Y. Wu, H. Wang, L. Gu, J. Zhang, Y. Qi, L. Meng, N. Kong and Y. Chai, Lanthanide Luminescence Nanothermometer with Working Wavelength beyond 1500 Nm for Cerebrovascular Temperature Imaging in Vivo, *Nat. Commun.*, 2024, **15**(1), 2341.

54 M. Yangui, K. Saidi, C. Hernández-Álvarez, M. Dammak and I. R. Martín, Ratiometric Luminescent Thermometry with Excellent Sensitivity in the Visible and Near-Infrared (NIR-II/III) Based on Thermally Coupled and Non-Thermally Coupled Energy Levels of Er^{3+} and Ho^{3+} Ions, *J. Alloys Compd.*, 2025, **1010**, 177958, DOI: 10.1016/j.jallcom.2024.177958.

55 H. Lv, Q. Wu, L. Luo, W. Li and P. Du, Thermochromic Upconversion Emission in Tm^{3+}/Yb^{3+}-Codoped $La_2Mo_3O_{12}$ Microparticles *via* Negative Thermal Expansion Engineering for Ultrahigh Sensitivity Optical Thermometry, *J. Phys. Chem. C*, 2023, **127**(7), 3808–3818, DOI: 10.1021/acs.jpcc.2c08527.

56 X. Ge, Q. Zhang, T. Fei, Y. Wu, L. Luo and P. Du, Designing Polychromatic Luminescence in Mn^{2+}-Doped Cs2NaLuCl6 Double Perovskite Crystals *via* Energy Transfer Engineering for Optical Thermometry and X-Ray Imaging, *Inorg. Chem.*, 2025, **64**(6), 3038–3047, DOI: 10.1021/acs.inorgchem.4c05370.

57 N. Ben Amar, K. Saidi, C. Hernández-Álvarez, M. Dammak and I. R. Martín, $Y_2Mo_4O_{15}$:$Er^{3+}/Tm^{3+}/Yb^{3+}$ Nanophosphors for High-Sensitivity Optical Temperature Sensing, *ACS Appl. Nano Mater.*, 2025, **8**(35), 17133–17143, DOI: 10.1021/acsanm.5c02804.

58 S. Liu, Z. An, J. Huang and B. Zhou, Enabling Efficient NIR-II Luminescence in Lithium-Sublattice Core—Shell Nanocrystals towards Stark Sublevel Based Nanothermometry, *Nano Res.*, 2023, **16**(1), 1626–1633, DOI: 10.1007/s12274-022-5121-9.

59 M. Runowski, P. Woźny, N. Stopikowska, I. R. Martín, V. Lavín and S. Lis, Luminescent Nanothermometer Operating at Very High Temperature—Sensing up to 1000 K with Upconverting Nanoparticles (Yb^{3+}/Tm^{3+}), *ACS Appl. Mater. Interfaces*, 2020, **12**(39), 43933–43941, DOI: 10.1021/acsami.0c13011.

60 K. Saidi, C. Hernández-Álvarez, M. Runowski, M. Dammak and I. Rafael Martín Benenzuela, Temperature and Pressure Sensing Using an Optical Platform Based on Upconversion Luminescence in $NaSrY(MoO_4)_3$ Codoped with Er^{3+} and Yb^{3+} Nanophosphors, *ACS Appl. Nano Mater.*, 2023, **6**(20), 19431–19442, DOI: 10.1021/acsanm.3c04031.

61 K. Soler-Carracedo, I. R. Martin, M. Runowski, L. L. Martín, F. Lahoz, A. D. Lozano-Gorrín and F. Paz-Buclatin, Luminescent Nd^{3+}-Based Microresonators Working as Optical Vacuum Sensors, *Adv. Opt. Mater.*, 2020, **8**(19), 2000678, DOI: 10.1002/adom.202000678.